The Astronomical Journal, 166:93 (9pp), 2023 September https://doi.org/10.3847/1538-3881/ace52b

Dynamical Masses of 20 Asteroids Determined with Gaia DR3 Asteroid Observations

Fan Li (李凡)[1], Ye Yuan (袁烨)[1,2], Yanning Fu (傅燕宁)[1], and Jian Chen (陈健)[1,3]
[1] Purple Mountain Observatory, Chinese Academy of Sciences, Nanjing 210023, People's Republic of China; lifan@pmo.ac.cn
[2] CAS Center for Excellence in Comparative Planetology, Hefei 230026, People's Republic of China
[3] School of Astronomy and Space Sciences,University of Science and Technology of China, Hefei 230026, People's Republic of China
Received 2022 October 11; revised 2023 July 3; accepted 2023 July 5; published 2023 August 4

Abstract

We combined the ground-based and Gaia Data Release 3 (DR3) asteroid observations to determine the masses of 20 asteroids with asteroid–asteroid close encounters. In order to take full advantage of the high-precision observations from Gaia, we use the Fisher information to select appropriate model parameters and the modified Encke's equation of motion to construct a dynamical model complete at the level of observation precision. With diameters from literature, bulk densities of 20 asteroids are derived. The results indicate that the utilization of Gaia DR3 provides substantial benefits in terms of improving mass precision. Among the 20 asteroids analyzed in our study, we find that 10 asteroids achieved a mass precision better than 5%, and 15 asteroids better than 10%.

Unified Astronomy Thesaurus concepts: Asteroids (72); Astrometry (80); Celestial mechanics (211); Close encounters (255)

1. Introduction

Density is a fundamental parameter to restrict asteroid composition and internal structure, while mass is the bottleneck for deriving it (Carry 2012). Asteroid masses are also useful for constructing high-precision solar system gravitational fields, which is crucial in deep space exploration. In addition, the uncertainty of the Mars ephemeris, and so that of its gravitational field, is mainly resulted from the mass uncertainty of main-belt asteroids (Standish 2000; Fienga et al. 2009).

Asteroid mass determination with close encounter is a widely used method that gives more than 948 individual determinations for 158 asteroids (Carry 2012; Goffin 2014; Kretlow 2020). This method determines the mass of a massive asteroid through its gravitational perturbation on the orbit of a massless asteroid, often called a test particle. For massive dwarf planets or main-belt asteroids, such as (1) Ceres, (2) Pallas, (4) Vesta, and (10) Hygeia, accuracies of a few percent can be achieved. As the mass of the asteroid decreases, the relative precision of the determination decreases. Currently, there are about 103 asteroids with mass precision better than 20% (query from SiMDA catalog;[4] Kretlow 2020). Therefore, improving the precision of the observations and the precision of the background gravitational field model is essential to continuously improve the precision of asteroid mass determination. When both the background field and the observations are given, the precision of mass determination can still be improved by developing new algorithms and promoting the accuracy of the historical observations. For example, some researchers use simultaneous mass determination (Goffin 2014) or a Markov Chain Monte Carlo algorithm to improve the fitting process (Siltala & Granvik 2017, 2022a).

Gaia is a space telescope launched by ESA in 2013 (Gaia Collaboration et al. 2016). Although the primary mission of Gaia is to perform high-precision astrometry of Milky Way stars, it also observes some asteroids in the solar system. Gaia Data Release 3 (DR3) was published on 2022 June 13, releasing 23,336,467 observations made in 33 months from August 2014 on 158,152 objects in the solar system (Gaia Collaboration et al. 2023; Tanga et al. 2023). Compared with ground-based observations, Gaia observations are very precise.

The high precision of Gaia observations is helpful, especially for determining some weak perturbations, e.g., the perturbation due to asteroid–asteroid encounter.

The sensitivity of calculated observations to the to-be-determined mass depends on the selection of the initial epoch, at which the epoch state of an asteroid is part of fitting parameter set. (Carpino & Knezevic 1996). And the selection should be made according to the available observations. In the case when observations have similar precision, the time distribution of observations can be used to select the initial epoch such that the sensitivity is high (Li et al. 2019). In the case of combining Gaia and ground-based observations, the precision distribution of observations should also be taken into consideration. Moreover, we should consider a complete dynamical model rather than uniformly fixed ones. A complete dynamical model includes all perturbations that could lead to changes in the observables up to the observational precision, which means a different model for different close encounters. Specifically, we will take advantage of modified Encke's equation of motion to screen perturbations to construct a dynamical model complete at the level of observation precision, use Fisher information to improve the selection of appropriate model parameters, and combine ground-based observations and the observations from Gaia DR3 to determine the mass of asteroids. Finally, we obtain the masses of 20 asteroids.

The structure of this paper is as follows: Section 2 introduces the method, including constructing a completely dynamical model based on the modified Encke's equation of motion and using Fisher information in selecting appropriate model parameters. Section 3 gives the information and observations involving the close encounter event of three asteroids.

[4] https://astro.kretlow.de/simda/

Section 4 presents the results and discussion. Section 5 gives the conclusions.

2. Method

Asteroid mass M can be determined from observational positions of an encountering test particle by a least-squares method. The objective function is

$$\chi^2 = \boldsymbol{\xi}^T W \boldsymbol{\xi},$$

where $\boldsymbol{\xi}$ is the residual (the observed position minus the computed position) and W is the weight matrix. The computed position depends on M and the six-dimensional state $\boldsymbol{s}$ of the test particle at the initial epoch. The weight matrix is usually taken as $W = \Gamma^{-1}$, where Γ is the error matrix. For a perturber with multiple encounters, the weighted average was calculated. We then check if this averaged value falls within the 3σ boundaries of the separately determined values. If it does not, we exclude the result. Otherwise, the averaged value is taken as the finally determined mass of the perturber.

2.1. Selecting Appropriate Model Parameters by Fisher Information

Given a probability density distribution $f(X|\theta)$ of a random variable X with a parameter θ, the Fisher information refers to the information that X contains about the parameter θ (Lehmann & Casella 1998; Ly et al. 2017). When fitting a model to observations, with Gaussian errors, the likelihood function is $L(\theta|x) = f(x;\theta) = \exp(-\frac{\chi^2}{2})$, and we then define the score function $s(\theta) = \frac{\partial \ln f(x;\theta)}{\partial \theta}$. The Fisher information is defined to be the variance of the score, that is,

$$\begin{aligned} I(\theta) &= \boldsymbol{Var}[s(\theta)] \\ &= \boldsymbol{E}[s^2(\theta)] - (\boldsymbol{E}[s(\theta)])^2 \\ &= \boldsymbol{E}\left[\left(\frac{\partial \ln f}{\partial \theta}\right)^2\right], \end{aligned} \tag{1}$$

where E and Var denotes the expectation and variance operator, respectively. When f can be differentiated to the second order, we have

$$I(\theta) = -\boldsymbol{E}\left[\frac{\partial^2 \ln f}{\partial \theta^2}\right]. \tag{2}$$

Then, the Fisher information is the expectation of the negative second-order derivative of the log-likelihood function at the true value of the parameter.

As noted in Li et al. (2019), different initial epoch t_0 implies different model parameters, i.e., $\boldsymbol{x} = (M, \boldsymbol{s}(t_0)^{\mathrm{T}})^{\mathrm{T}}$, and thus the functional dependence of observables on model parameters changes with the initial epoch t_0. In order to determine M as precise as possible with given observations, we select t_0 such that the Fisher information contained in observations on mass (Tegmark 1997; Ly et al. 2017)

$$I(M, t_0) = \frac{1}{2}\boldsymbol{E}\left[\frac{\partial^2 \chi^2}{\partial M^2}\right], \tag{3}$$

takes its maximum value in a time interval, e.g., the one spanned by observations. Assuming that the nominal value of M is M_0, which comes from DE440 (Park et al. 2021), we have

$$\begin{aligned} I(M_0, t_0) &= \frac{1}{2}\boldsymbol{E}\left[\frac{\partial^2 \chi^2}{\partial M^2}\right]\Bigg|_{M=M_0} \\ &= \frac{1}{2}\frac{\partial^2 (\boldsymbol{C}_{M_0} - \boldsymbol{C}_M)^T (\boldsymbol{C}_{M_0} - \boldsymbol{C}_M)}{\partial M^2} \\ &= \frac{1}{2}\frac{\partial^2 \chi^2_{M_0}}{\partial M^2}, \end{aligned} \tag{4}$$

where $\boldsymbol{C}_M$ denotes mass is set to M when calculating computed position. A second-order central difference approximation is used to numerically calculate $I(M_0, t_0)$. A grid search method is used to solve the optimization problem. The grid interval decreases is set as 1 day. Additionally, the epoch of closest encounter is added as a grid point. Because the Fisher information changes rapidly at this epoch. At other epochs, it changes slowly. A typical example is show on Figure 1. We have found that Fisher information behaves similarly to Figure 1 in each of the close encounters we study, confirming that the time resolution is sufficient, the only exception is the epoch of closest encounter, which is manually added as a grid point.

Figure 1 gives I as function of t_0 for the (52) Europa and 88979 close encounter. Comparing the Fisher information curves including all observations with that considering only the ground-based observations, we see that both of them show large variations near the close encounter. In addition, introducing Gaia observations not only increases the Fisher information significantly, but may also changes the time of I's maximum. When Gaia observations, whose precision is about milliarcsecond and period is located from 2014 November to 2017 March, are included, it changes the trend of Fisher information and thus affects the time of I's maximum.

2.2. Constructing a Complete Dynamical Model Based on the Modified Encke's Equation of Motion

Asteroid dynamical model is the basis for numerical integration to obtain the positions of asteroids. The dynamical model used by Jet Propulsion Laboratory (JPL) Horizons to produce the asteroids ephemerides (hereafter referred to as the JPL model) takes into account the gravitational forces of the Sun, the eight planets, Pluto, and so called Big16 (the 16 massive asteroids in the main belt), where the Sun, the eight planets, and Pluto are considered with relativistic corrections. Some researchers also consider the oblateness effect of the Sun and some large planets, the Yarkovsky effect (Farnocchia et al. 2021b, 2021a). In order to take into account as completely as possible the dynamical factors that affect the observables larger than their respective errors, we consider the gravitational forces of the Sun, the eight planets, the Moon, and Pluto as point masses with relativistic corrections. To save computation time, the 343 asteroids that modeled in DE440 planetary ephemerides (Park et al. 2021), the J2 of the Sun and of the eight planets are retained when the perturbation affecting the observables at the levels of observational errors.

The threshold for the observation precision is set to 1 mas for Gaia, 10 mas for ground-based observations after 2000, and 50 mas for ground-based observations before 2000 (Vereš et al. 2017). The effect of a perturbation is calculated using the modified Encke's equation of motion (Hernandez &

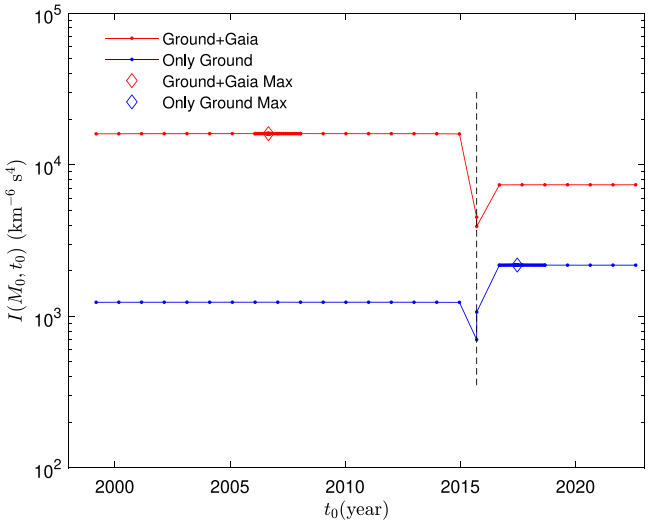

Figure 1. The change of Fisher information with initial epoch for the (52) Europa and 88979 close encounter is shown in red for using the ground-based and Gaia observations, and in blue for using only the ground-based observations, with the vertical dotted line indicating the encounter time. The addition of Gaia observations increases the Fisher information and also changes the moment of I's maximum.

Holman 2021), which allows direct estimation of the effect of a perturbation without integrating the whole model twice. Specifically, consider two dynamical models, the base model $\boldsymbol{f}(\boldsymbol{x}, t)$ and a more complete model $\hat{\boldsymbol{f}}(\boldsymbol{y}, t)$, differing by the perturbation $\boldsymbol{R}(\boldsymbol{x}, t)$,

$$\begin{aligned} \ddot{\boldsymbol{x}} &= \boldsymbol{f}(\boldsymbol{x}, t), \\ \ddot{\boldsymbol{y}} &= \hat{\boldsymbol{f}}(\boldsymbol{y}, t) = \boldsymbol{f}(\boldsymbol{y}, t) + \boldsymbol{R}(\boldsymbol{y}, t). \end{aligned} \tag{5}$$

We first integrate the base model; thus $\boldsymbol{x}$ is known. The orbital change caused by the perturbation $\boldsymbol{R}$ is $\boldsymbol{d} = \boldsymbol{y} - \boldsymbol{x}$; we have

$$\ddot{\boldsymbol{d}} = \boldsymbol{f}(\boldsymbol{x} + \boldsymbol{d}, t) - \boldsymbol{f}(\boldsymbol{x}, t) + \boldsymbol{R}(\boldsymbol{x} + \boldsymbol{d}, t). \tag{6}$$

In the solar system case, we consider an approximation to $\boldsymbol{f}(\boldsymbol{x}+\boldsymbol{d}, t) - \boldsymbol{f}(\boldsymbol{x}, t)$, i.e., neglecting higher-order terms as detailed below. For a typical main-belt asteroid (semimajor axis equals to 3 au), the gravitational acceleration difference caused by the Sun $|(\boldsymbol{a}(\boldsymbol{d}+\boldsymbol{x}) - \boldsymbol{a}(\boldsymbol{x})|$ is about $10^{-5} a_{\text{Sun}}$ at $d = 10000$ km (which is much smaller than those caused by (1) Ceres on a ordinary test particle in 60 yr, e.g., 2500 km for (9870) Maehata), the difference caused by the Jupiter is about $10^{-8} a_{\text{Sun}}$, the difference caused by the Saturn is about $10^{-10} a_{\text{Sun}}$, where a_{Sun} denotes the gravitational acceleration due to the Sun. While gravitational acceleration from (1) Ceres is about $10^{-8} a_{\text{Sun}}$. Therefore, neglecting terms that are 2 mag smaller than the acceleration of (1) Ceres gives

$$\boldsymbol{f}(\boldsymbol{x} + \boldsymbol{d}, t) - \boldsymbol{f}(\boldsymbol{x}, t) = \sum_i \Delta \boldsymbol{a}_i, \tag{7}$$

where

$$\Delta \boldsymbol{a}_i = -\frac{GM_i(\boldsymbol{d} + \boldsymbol{x}_i)}{|\boldsymbol{d} + \boldsymbol{x}_i|^3} + \frac{GM_i \boldsymbol{x}_i}{x_i^3},\ i \in \{\text{Sun, Jup}\}, \tag{8}$$

where $\boldsymbol{x}_i$ is the vector from i to the test particle and M_i is the mass of i. To avoid the difference of similar quantities in Equation (8), the following model can be obtained (see

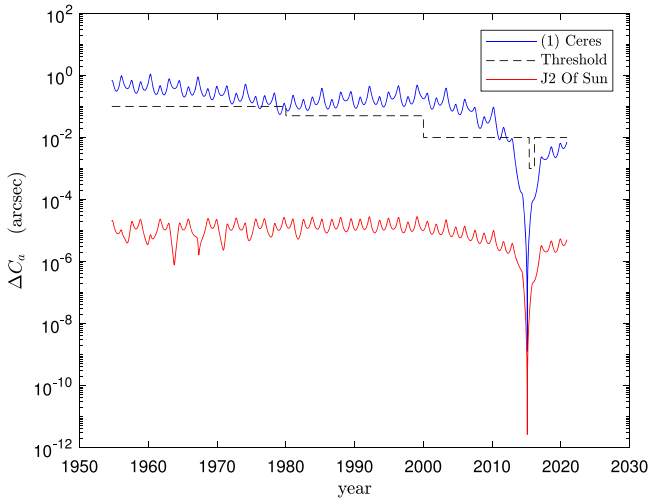

Figure 2. Observational effects from different perturbations for (9870) Maehata, where blue line indicates those caused by (1) Ceres and red is the solar J2 term. The dotted–dashed line indicates the observational precision threshold.

Hernandez & Holman 2021):

$$\begin{aligned} \ddot{\boldsymbol{d}} &= \sum_i \Delta \boldsymbol{a}_i + \boldsymbol{R}(\boldsymbol{x} + \boldsymbol{d}, t),\ i \in \{\text{Sun, Jup}\}, \\ \Delta \boldsymbol{a}_i &= -\frac{GM_i \boldsymbol{d}}{x_i^3} + \frac{GM_i}{x_i^3} g(q_i)(\boldsymbol{x}_i + \boldsymbol{d}), \\ g(q) &= q\frac{3 + 3q + q^2}{(1+q)^{3/2} + (1+q)^3}, \\ q_i &= \frac{(\boldsymbol{d} + 2\boldsymbol{x}_i) \cdot \boldsymbol{d}}{x_i^2}. \end{aligned} \tag{9}$$

The distance difference caused by the perturbation can be obtained by integrating Equations (9). Then angular distance can be derived by considering the distance between the Earth and the observed test particle. By comparing the angular distance with the observation precision threshold, we can determine whether the perturbation is necessary to be added to the dynamical model. Figure 2 shows, as a typical example, the case of (9870) Maehata. The blue line shows the effect of the (1) Ceres perturbation, while the red line shows the effect of the Sun J2 perturbation, from which the (1) Ceres perturbation needs to be considered while the Sun J2 perturbation can be ignored. In most of the case, for test particles with only ground-based observations, the JPL model is precise enough.

2.3. Astrometric Uncertainties of Gaia DR3 Observations

The Gaia satellite has been continuously scanning the sky since December 2013 (Gaia Collaboration et al. 2016, 2018a, 2023; Tanga et al. 2023). As the satellite keeps rotating, all sources on the focal plane drift continuously (in the along-scan direction, AL) across the different CCD strips. During each passage of the focal plane (known as a transit), the Astrometric Field instrument (AF) can provide a maximum of nine positions. The positions are initially expressed in pixels in the coordinate system (AL, AC) and then converted into R.A. and decl. with position angle. This leads to a strong correlation of uncertainties in the R.A. and decl.. Gaia team separated the uncertainties into two components: systematic and random. Systematic component is same for all positions within the same

transit, while random one statistically independent from one CCD to another. For the mth transit, the covariance matrix,

$$\Gamma_{tm} = \begin{pmatrix} \Gamma_1 & \mathbf{0} & \cdots & \mathbf{0} \\ \mathbf{0} & \Gamma_2 & \cdots & \mathbf{0} \\ \vdots & \vdots & \ddots & \\ \mathbf{0} & \mathbf{0} & \cdots & \Gamma_9 \end{pmatrix} + \begin{pmatrix} \Gamma_s & \Gamma_s & \cdots & \Gamma_s \\ \Gamma_s & \Gamma_s & \cdots & \Gamma_s \\ \vdots & \vdots & \ddots & \\ \Gamma_s & \Gamma_s & \cdots & \Gamma_s \end{pmatrix}, \tag{10}$$

where Γ_i is the random uncertainty of the AFi position, Γ_s is the systematic uncertainty of the transit, and $\mathbf{0}$ is a 2×2 matrix of zeros. For accuracy in the AC–AL plane, it reaches milliarcseconds in AL but hundreds of milliarcseconds in AC (Tanga et al. 2023). The R.A., decl., and position angle, as well as the Γ_i and Γ_s for every observation, are provided in Gaia DR3 (Tanga et al. 2023).

2.4. Weighting Scheme and Fitting

As usual, the weight of each observation is assigned according to its error. Therefore, the error matrix Γ writes

$$\Gamma = \begin{pmatrix} \Gamma_{\rm Gaia} & \mathbf{0} \\ \mathbf{0} & \Gamma_{\rm ground} \end{pmatrix}, \tag{11}$$

where

$$\Gamma_{\rm Gaia} = \begin{pmatrix} \Gamma_{t1} & \mathbf{0} & \cdots & \mathbf{0} \\ \mathbf{0} & \Gamma_{t2} & \cdots & \mathbf{0} \\ \vdots & \vdots & \ddots & \vdots \\ \mathbf{0} & \mathbf{0} & \cdots & \Gamma_{tm} \end{pmatrix},$$

$$\Gamma_{\rm ground} = \begin{pmatrix} \sigma_1^2 & 0 & \cdots & 0 \\ 0 & \sigma_2^2 & \cdots & 0 \\ \vdots & \vdots & \ddots & \vdots \\ 0 & 0 & \cdots & \sigma_{2n}^2 \end{pmatrix}. \tag{12}$$

m denotes the transit number of Gaia observations, while n denotes the number of ground-based observations. $\Gamma_{\rm Gaia}$ is directly taken from the DR3 (Tanga et al. 2023). $\Gamma_{\rm ground}$ is taken from AstDyS (Vereš et al. 2017).[5] In the fitting process, ground-based observations of which the residuals with respect to JPL solutions are great than 3σ are rejected. For Gaia observations, no data were removed because the Gaia data processing team had filtered the data and found only 0.58% of the data being outliers (Tanga et al. 2023).

For ground-based observations, the catalog bias are considered (Farnocchia et al. 2015). Following Siltala & Granvik (2022a), those measurements that could not be debiased are rejected. And for Gaia observations, a relativistic light bending correction are applied (Urban & Seidelmann 2014; Tanga et al. 2023). The photocenter shifts are not considered, because the test particles are small (less than 20 km based on the absolute magnitude) and the shifts are less than 0.02 mas at 1 au.

An orthogonal decomposition of the real symmetric matrix Γ is performed. That is, the orthogonal matrix R is found with a diagonal matrix Λ such that $\Gamma = R\Lambda R^T = (R\Lambda^{1/2})(R\Lambda^{1/2})^T = PP^T$. After obtaining the decomposition of Γ, it is sufficient to do the variable substitution such that

$$\boldsymbol{\xi}' = P^{-1}\boldsymbol{\xi}, \tag{13}$$

then the objective function becomes

$$\chi^2 = \boldsymbol{\xi}'^T\boldsymbol{\xi}', \tag{14}$$

a homogeneous quadratic polynomial without cross terms. In addition, the initial guesses of the state parameters in the model parameters are obtained from JPL Horizons.[6] And the initial guesses of the M are varied uniformly from 0 to $2M_{\rm jpl}$ in steps of $0.1M_{\rm jpl}$ (a total of 21 guesses).

3. Close Encounter Information and Observations

The close encounters potentially helpful in the determination of asteroid mass are given in Tang et al. (2017). We selected encounters for which Gaia DR3 observations are available and the predicted precision given in Tang et al. (2017) is better than 10%. Table 1 gives the information about the encountering test particles with Gaia. Each relevant encounter, the time span and the number of observations covered by the ground-based and Gaia observations are given in Table 2, together with the maximum Fisher information and the time when it reaches the maximum value.

The observations are mainly from AstDyS and Gaia DR3, and also contain a portion of our observations. We observed (1764) Cogshall using Yaoan High Precision Telescope (Yuan et al. 2021) from 2019 January to 2021 April, acquiring 569 observations over 66 nights. Observations are made in the *Rc* or *Ic* band, and the exposure time varies from 30 to 60 s depending on the weather and target brightness. The specifications of Yaoan High Precision Telescope and camera are shown in Table 3. The observations[7] are processed with MAAT (Ofek 2014) and using Gaia DR2 (Gaia Collaboration et al. 2018b) as a reference catalog, for details see Yuan et al. (2021).

4. Results and Discussion

Table 4 gives the determined masses using Gaia and ground-based observations, as well as the root mean square of the residuals of the ground-based observations in R.A. $\sigma_{\Delta\alpha\cos\delta}$ and decl. $\sigma_{\Delta\delta}$, and Gaia observations in AC $\sigma_{\Delta\rm AC}$ and AL $\sigma_{\Delta\rm AL}$, respectively. Among the 20 perturbers involved in this work, 15 perturbers have only one encounter and five have two close encounters. For multi-encounter cases, some previous studies (Goffin 2014; Baer & Chesley 2017; Siltala & Granvik 2017, 2022a) performed simultaneously fitting to all available observations of two or more different test particles. Moreover, some additionally include fitting to the observations of the perturber, considering the error introduced by their orbits. Despite the fact that these approaches can improve precision, we use a relatively simple but efficient approach described in Section 2. We calculated the weighted average of the separately determined masses. This method allows for a mutual compatibility between masses determined with independent observations. As shown by Baer & Chesley (2017), simultaneous solutions for non-gravitationally coupled asteroids did not yield significant benefits. At this point, it should point out that the maximum mass ratio is 0.008, which is the case of (445) Enda encounter with (1764) Cogshall. For other cases, the mass ratio is much smaller. So, it is still appropriate to perform fittings separately for each encounter. However, as

[5] https://newton.spacedys.com/astdys

[6] https://ssd.jpl.nasa.gov/horizons/

[7] https://nadc.china-vo.org/res/r101250/

Table 1
Close Encounters Used in the Present Paper

Perturber	Test Particle	T_{enc} yyyy-mm-dd	D_{enc} km	V_{enc} km s^{-1}	Deflection mas
(3) Juno	48718	2018-01-17	86343.10	5.60	247.55
(8) Flora	19293	2013-02-18	547549.45	0.76	346.27
(9) Metis	191683	2013-03-6	561717.86	2.70	48.79
(9) Metis	143451	2017-09-18	216190.76	2.19	192.96
(11) Parthenope	196434	2010-12-18	437141.88	2.79	72.42
(11) Parthenope	112061	2011-02-26	439105.95	1.44	269.22
(15) Eunomia	84417	2009-09-9	540254.76	1.80	495.73
(15) Eunomia	5199	2015-06-16	405595.13	5.69	65.97
(19) Fortuna	58486	2017-02-14	394419.57	4.29	26.35
(19) Fortuna	79699	2019-08-25	478844.38	1.08	340.31
(24) Themis	83354	2013-12-12	207732.20	4.51	83.07
(29) Amphitrite	9870	2015-02-3	228958.05	4.08	96.03
(45) Eugenia	50391	2012-12-14	349647.92	0.91	537.06
(48) Doris	181181	2019-09-16	163655.58	2.24	572.49
(52) Europa	88978	2015-09-14	285549.57	2.99	179.69
(88) Thisbe	26094	2016-10-13	620397.48	1.28	467.25
(88) Thisbe	88021	2019-05-11	288025.27	1.65	608.44
(94) Aurora	115559	2018-07-11	691915.13	1.10	284.63
(110) Lydia	66778	2010-03-22	16128.74	1.61	625.95
(223) Rosa	35525	2010-12-31	53559.78	2.04	115.07
(308) Polyxo	70464	2009-07-9	154265.32	1.83	258.97
(389) Industria	33537	2011-08-3	16875.54	2.50	109.02
(445) Edna	1764	2014-10-31	6483.27	8.23	48.55
(471) Papagena	238319	2016-08-30	672146.67	1.93	62.63
(712) Boliviana	222643	2009-02-16	221142.45	2.59	62.57

observation precision improves, more cases involving gravitationally coupled asteroids will arise. So, in the future, we will implement a procedure for simultaneously fitting to all observations, considering a dynamical model appropriate in the whole observation time span.

We adopt the diameters of (3) Juno, (8) Flora, (9) Metis, (11) Parthenope, (15) Eunomia, (19) Fortuna, (24) Themis, (29) Amphitrite, (45) Eugenia, (48) Doris, (52) Europa, (88) Thisbe obtained by Vernazza et al. (2021), based on VLT/SPHERE imaging. The diameters of the other asteroids, namely (94) Aurora, (110) Lydia, (223) Rosa, (389) Industria, (445) Edna, (471) Papagena and (712) Boliviana, are from SiMDA (Kretlow 2020), which are weighted averages of other studies. The diameter value for (308) Polyxo, obtained from Masiero et al. (2014), is not included in the SiMDA. The final results of the masses determined in this paper and the derived bulk densities, as well as the diameters and the references are given in Table 5.

4.1. Overall Views of the Masses and Bulk Densities

Figure 3 is a histogram of the precision of mass determination; the blue one indicates the result of this work and the orange one indicates the result from SiMDA. In this work, 10 asteroids' masses are determined better than 5%. Figure 4 is a plot of mass versus bulk density for 20 asteroids, with the color depth representing the precision of mass determination and the size of the circle representing the diameter. Among the 20 asteroids studied by this work, 11 asteroids have new mass uncertainty smaller than other independent determinations from SiMDA, 18 asteroids have new mass within SiMDA's 3σ boundaries, and 12 have new mass within 1σ. 19 new bulk densities by this work are in 3σ boundaries of bulk densities from SiMDA and 14 are in 1σ. Compared with the bulk densities by Carry (2012), 13 bulk densities are in their 3σ boundaries and eight are in their 1σ; five asteroids are not included in Carry (2012).

4.2. Discussions on Bulk Density and Its Application for Some Asteroids

(15) Eunomia is an S-type main-belt asteroid. In our study, its mass is determined to be $2.69 \pm 0.05 \times 10^{19}$ kg. However, there is a notable discrepancy between our result and the mass reported by Siltala & Granvik (2022a), which is $3.03 \pm 0.10 \times 10^{19}$ kg determined with DR2. The differences between these results may arise from differences in observations, planetary ephemerides, and dynamical models used in the studies. The reduction in uncertainty from 0.1×10^{19} kg (Siltala & Granvik 2022a) to 0.05×10^{19} kg demonstrates the improvement brought by Gaia DR3 compared with DR2. Using the new mass obtained in this study, we can calculate the bulk density of (15) Eunomia to be 2.61 ± 0.10 g cm^{-3}, with a relative error of 3.8%. The derived bulk density is lower than the expectations of asteroid of its diameter based on the relation from Figure 9 in Carry (2012). We assume a grain density of ordinary chondrites for S-type asteroids, 3.26 g cm^{-3} (Masiero et al. 2014), which would imply a macroporosity of 20% with Equation (15) from Carry (2012):

$$P = 100\%\left(1 - \frac{\rho}{\rho_m}\right), \tag{15}$$

where ρ is the bulk density and ρ_m is the grain density of the constituent minerals. Michel et al. (2004) suggests that (15) Eunomia is a reaccumulation of most of the fragments of a

Table 2
Observations Used in the Present Paper

Perturber	Test Particle	T_{enc}	Observation Period	Number	I	Inital Epoch
(3) Juno	48718	2018-01-17	(1996-09-13, 2022-07-16)	1223	303763	2018-02-5 00:00:00.00
			(2014-09-19, 2017-05-3)[a]	197[a]		
(8) Flora	19293	2013-02-18	(1996-07-18, 2022-04-28)	1197	2397424	1996-07-21 08:50:50.18
			(2014-10-21, 2016-08-10)[a]	301[a]		
(9) Metis	191683	2013-03-6	(2000-08-26, 2022-06-29)	614	561284	2000-08-27 08:39:41.43
			(2015-09-7, 2017-03-25)[a]	111[a]		
(9) Metis	143451	2017-09-18	(1992-11-27, 2022-06-16)	598	25903	2018-01-19 00:00:00.00
			(2015-11-15, 2017-04-14)[a]	89[a]		
(11) Parthenope	196434	2010-12-18	(1999-06-15, 2022-03-23)	776	480475	1999-06-17 07:38:17.34
			(2015-01-24, 2016-07-7)[a]	220[a]		
(11) Parthenope	112061	2011-02-26	(1997-02-7, 2022-11-1)	772	1685028	2011-02-23 00:00:00.00
			(2014-12-13, 2016-09-11)[a]	93[a]		
(15) Eunomia	84417	2009-09-9	(1995-03-8, 2022-04-28)	1215	4116039	2009-01-30 00:00:00.00
			(2015-05-25, 2017-04-15)[a]	207[a]		
(15) Eunomia	5199	2015-06-16	(1990-10-22, 2022-06-21)	3179	27670	1990-10-23 09:28:23.10
			(2014-08-31, 2017-05-8)[a]	182[a]		
(19) Fortuna	58486	2017-02-14	(1994-02-04, 2022-01-26)	768	10141	2017-03-3 00:00:00.00
			(2015-02-7, 2017-01-6)[a]	89[a]		
(19) Fortuna	79699	2019-08-25	(1998-09-18, 2022-05-26)	1371	926012	2021-08-14 00:00:00.00
			(2015-02-14, 2017-01-2)[a]	79[a]		
(24) Themis	83354	2013-12-12	(1999-03-22, 2022-11-2)	1084	81818	2013-11-23 00:00:00.00
			(2014-08-18, 2017-01-3)[a]	180[a]		
(29) Amphitrite	9870	2015-02-3	(1990-10-22, 2022-11-7)	2876	6968776	1990-10-23 09:59:24.45
			(2015-05-8, 2017-05-18)[a]	329[a]		
(45) Eugenia	50391	2012-12-14	(1996-06-10, 2022-05-26)	2276	35700850	1996-06-11 07:28:27.53
			(2014-09-09, 2017-05-4)[a]	382[a]		
(48) Doris	181181	2019-09-16	(1999-09-09, 2022-11-1)	862	425869	2022-08-31 00:00:00.00
			(2015-02-23, 2016-11-19)[a]	66[a]		
(52) Europa	88978	2015-09-14	(1999-03-9, 2022-09-23)	1399	16062	2006-09-1 00:00:00.00
			(2014-09-02, 2017-03-11)[a]	111[a]		
(88) Thisbe	26094	2016-10-13	(1996-04-17, 2022-09-19)	2100	362623	2018-05-30 00:00:00.00
			(2014-11-3, 2017-05-23)[a]	165[a]		
(88) Thisbe	88021	2019-05-11	(2000-09-24, 2022-06-28)	923	351792	2022-04-25 00:00:00.00
			(2014-09-2, 2017-05-24)[a]	72[a]		
(94) Aurora	115559	2018-07-11	(1998-11-16, 2022-06-20)	768	162200	2018-09-11 00:00:00.00
			(2014-10-15, 2016-05-15)[a]	73[a]		
(110) Lydia	66778	2010-03-22	(1993-03-23, 2022-04-26)	776	1026130036	1993-04-16 00:00:00.00
			(2015-03-28, 2017-03-1)[a]	129[a]		
(223) Rosa	35525	2010-12-31	(1990-09-25, 2022-05-04)	1541	44539585	2010-11-14 00:00:00.00
			(2014-09-17, 2017-05-14)[a]	134[a]		
(308) Polyxo	70464	2009-07-09	(1995-10-26, 2022-06-2)	1246	3967339	2009-04-06 00:00:00.00
			(2015-06-25, 2017-04-15)[a]	92[a]		
(389) Industria	33537	2011-08-03	(1994-01-16, 2022-07-27)	1733	515648723	1994-01-18 13:18:26.78
			(2014-08-05, 2017-03-6)[a]	185[a]		
(445) Edna	1764	2014-10-31	(1990-08-16, 2022-11-6)	4446	472049096	1995-05-28 00:00:00.00
			(2014-09-19, 2017-05-19)[a]	307[a]		
(471) Papagena	238319	2016-08-30	(2003-12-23, 2022-04-09)	376	3954	2016-08-31 00:00:00.00
			(2015-04-29, 2016-02-25)[a]	43[a]		
(712) Boliviana	222643	2009-02-16	(2000-08-3, 2022-11-6)	529	2231283	2005-07-16 00:00:00.00
			(2014-11-25, 2015-03-13)[a]	100[a]		

Note.
[a] denotes Gaia observations.

completely shattered parent body. The macroporosity we get implies a rubble pile and conform with Michel et al. (2004).

(29) Amphitrite is an S-type main-belt asteroid. The newly determined mass falls in the 1σ boundaries from SiMDA and is consistent with the value provided by Siltala & Granvik (2022a), which was determined using Gaia DR2 data. The reduction in uncertainty from 3.2×10^{17} kg (Siltala & Granvik 2022a) to 2.2×10^{17} kg demonstrates the improvement brought by Gaia DR3 compared with DR2. The new derived

Table 3
Specifications of YAHPT

Parameter	Value
Diameter	0.8 m
Focal Length	8 m
Field of View	$11' \times 11'$
Pixel Scale	0.346 arcsec pixel $^{-1}$
CCD Pixels	2048×2048

Table 4
Root Mean Square of Residuals and Determined Mass for Every Encounter

Perturber (1)	Test Particle (2)	M (kg) (3)	σ_M (kg) (4)	$\sigma_{\Delta\alpha\cos\delta}$(arcsec) (5)	$\sigma_{\Delta\delta}$(arcsec) (6)	$\sigma_{\Delta AL}$(arcsec) (7)	$\sigma_{\Delta AC}$(arcsec) (8)
(3) Juno	48718	2.75×10^{19}	0.05×10^{19}	0.49	0.53	0.0048	0.18
(8) Flora	19293	4.61×10^{18}	0.22×10^{18}	0.41	0.42	0.0052	0.17
(9) Metis	191683	7.16×10^{18}	0.87×10^{18}	0.47	0.43	0.0046	0.17
(9) Metis	143451	6.06×10^{18}	0.29×10^{18}	0.39	0.39	0.0046	0.20
(11) Parthenope	196434	6.62×10^{18}	0.99×10^{18}	0.42	0.47	0.0085	0.32
(11) Parthenope	112061	6.37×10^{18}	0.66×10^{18}	0.40	0.38	0.0059	0.15
(15) Eunomia	84417	2.93×10^{19}	0.08×10^{19}	0.41	0.45	0.0044	0.23
(15) Eunomia	5199	2.58×10^{19}	0.06×10^{19}	0.34	0.37	0.0021	0.25
(19) Fortuna	58486	1.13×10^{19}	0.14×10^{19}	0.48	0.50	0.0055	0.18
(19) Fortuna	79699	7.27×10^{18}	0.70×10^{18}	0.42	0.44	0.0056	0.33
(24) Themis	83354	8.30×10^{18}	0.65×10^{18}	0.39	0.44	0.0064	0.21
(29) Amphitrite	9870	1.26×10^{19}	0.02×10^{19}	0.46	0.43	0.0020	0.20
(45) Eugenia	50391	5.95×10^{18}	0.11×10^{18}	0.41	0.43	0.0042	0.32
(48) Doris	181181	6.71×10^{18}	0.85×10^{18}	0.38	0.41	0.0062	0.14
(52) Europa	88978	2.76×10^{19}	0.03×10^{19}	0.42	0.43	0.0048	0.17
(88) Thisbe	26094	5.57×10^{18}	0.65×10^{18}	0.49	0.44	0.0045	0.21
(88) Thisbe	88021	8.49×10^{18}	0.58×10^{18}	0.44	0.48	0.0069	0.17
(94) Aurora	115559	3.22×10^{18}	0.91×10^{18}	0.42	0.44	0.0057	0.15
(110) Lydia	66778	1.37×10^{18}	0.02×10^{18}	0.40	0.42	0.0061	0.34
(223) Rosa	35525	9.48×10^{16}	6.98×10^{16}	0.44	0.47	0.0070	0.27
(308) Polyxo	70464	3.05×10^{18}	0.26×10^{18}	0.36	0.41	0.0067	0.27
(389) Industria	33537	6.80×10^{17}	0.24×10^{17}	0.44	0.47	0.0046	0.23
(445) Edna	1764	5.24×10^{17}	0.11×10^{17}	0.40	0.39	0.0013	0.15
(471) Papagena	238319	3.49×10^{18}	1.30×10^{18}	0.37	0.42	0.0037	0.35
(712) Boliviana	222643	1.66×10^{18}	0.61×10^{18}	0.47	0.46	0.0055	0.16

bulk density is consistent with expectations for an S-type asteroid (Carry 2012).

(52) Europa is classified as a C-type asteroid. The new determined mass, $2.755 \pm 0.029 \times 10^{19}$ kg, falls within SiMDA's 2σ boundaries. The relative error is 1.0%. Previous mass determinations by Siltala & Granvik (2022a) and Siltala & Granvik (2022b) using Gaia DR2 and DR3 data, respectively, reported masses of $2.9627 \pm 0.0736 \times 10^{19}$ kg and $3.011 \pm 0.0219 \times 10^{19}$ kg. Our uncertainty is comparable to Siltala & Granvik (2022b). And, our determined mass aligns more closely with SiMDA's value compared to Siltala & Granvik (2022a) and Siltala & Granvik (2022b). The new derived bulk density falls within the expected range based on its diameter, as shown in Figure 9 of Carry 2012. Assuming a grain density of 2.25 g cm^{-3} according to Carry 2012, we get a macroporosity of 28%.

(88) Thisbe is classified as a B-type asteroid. The derived bulk density of 1.33 ± 0.10 g cm^{-3} is compatible with the diameter–density relation observed for C-type asteroids (as shown in Figure 9 of Carry 2012). Notably, according to Carry (2012), the grain density of (88) Thisbe is reported to be 2.79 g cm^{-3}. A macroporosity of 52% can be calculated, which would imply a ripple rile structure. This result differs significantly from those by Carry (2012), which suggested a macroporosity of approximately 0%.

(223) Rosa is a proposed flyby target of the JUICE mission (Avdellidou et al. 2021). Although our uncertainty is almost 1 order of magnitude smaller than Kretlow (2022), the relative precision (74%) is still large. Moreover, our derived bulk density, 0.26 ± 0.19 g cm^{-3}, is smaller than Kretlow (2022) at their 2σ level. Avdellidou et al. (2021) propose that Rosa forms beyond the snow line and then migrates to the main belt. This is consistent with the low derived density. The flyby of the JUICE mission can be expected to refine further the mass and the density.

(308) Polyxo is classified as a T-type asteroid. According to Hiroi et al. (2003), Tagish lake meteorite maybe a part of 308 Polyxo. And, the bulk density of the Tagish Lake meteorite is reported to be 1.5 g cm^{-3} (Brown et al. 2000). The new bulk density of (308) Polyxo derived from our study is significantly higher than the bulk density of the Tagish Lake meteorite, with a difference of approximately 5σ. This suggests that the Tagish Lake meteorite may not be a part of (308) Polyxo. Instead, it is possible that the Tagish Lake meteorite belongs to other asteroids, as suggested by Hiroi et al. (2001).

(445) Edna is a C-type asteroid. The new determined mass, $5.24 \pm 0.11 \times 10^{17}$ kg, falls in the 1σ boundaries of SiMDA, and the relative error is 2.1%. However, there is a notable discrepancy between our result and the mass reported by Siltala & Granvik (2022a) and Siltala & Granvik (2022b), which is $3.561 \pm 0.189 \times 10^{17}$ kg and $3.551 \pm 0.0082 \times 10^{17}$ kg, respectively, using DR2 and DR3. The reasons for the different results are similar to those of (15) Eunomia. The difference in uncertainty between our study and the results by Siltala & Granvik (2022a) highlights the effect of using Gaia DR3 compared to DR2. Our result is closer to the value of 5.73×10^{17} kg given by Park et al. (2021). Our derived bulk density falls in the distribution interval of C-type asteroids (1.3 to 2.9 g cm^{-3}) according to Carry (2012). Additionally, according to Carry (2012), the associated meteorite of (445) Edna is CM carbonaceous chondrites, which correspond to a grain density of 2.25 ± 0.08 g cm^{-3}. Comparing our derived

Table 5
All Determined Masses and Derived Bulk Densities in the Present Paper

Perturber	$M \pm \sigma_M$ (kg)	σ_M/M (%)	$\rho \pm \sigma_\rho$ (g cm^{-3})	$D \pm \sigma_D$ (km)	Diameter Reference
(1)	(2)	(3)	(4)	(5)	(6)
(3) Juno	$2.75 \pm 0.05 \times 10^{19}$	1.9	3.20 ± 0.10	254 ± 2	Vernazza et al. (2021)
(8) Flora	$4.61 \pm 0.22 \times 10^{18}$	4.8	2.83 ± 0.18	146 ± 2	Vernazza et al. (2021)
(9) Metis	$6.18 \pm 0.28 \times 10^{18}$	4.5	2.28 ± 0.13	173 ± 2	Vernazza et al. (2021)
(11) Parthenope	$6.45 \pm 0.55 \times 10^{18}$	8.5	3.72 ± 0.35	149 ± 2	Vernazza et al. (2021)
(15) Eunomia	$2.69 \pm 0.05 \times 10^{19}$	1.7	2.61 ± 0.10	270 ± 3	Vernazza et al. (2021)
(19) Fortuna	$8.11 \pm 0.62 \times 10^{18}$	7.7	1.65 ± 0.13	211 ± 2	Vernazza et al. (2021)
(24) Themis	$8.30 \pm 0.65 \times 10^{18}$	7.9	1.76 ± 0.16	208 ± 3	Vernazza et al. (2021)
(29) Amphitrite	$1.26 \pm 0.02 \times 10^{19}$	1.8	2.83 ± 0.10	204 ± 2	Vernazza et al. (2021)
(45) Eugenia	$5.95 \pm 0.11 \times 10^{18}$	1.9	1.71 ± 0.06	188 ± 2	Vernazza et al. (2021)
(48) Doris	$6.71 \pm 0.85 \times 10^{18}$	12.6	1.29 ± 0.17	215 ± 3	Vernazza et al. (2021)
(52) Europa	$2.76 \pm 0.03 \times 10^{19}$	1.0	1.62 ± 0.06	319 ± 4	Vernazza et al. (2021)
(88) Thisbe	$7.20 \pm 0.43 \times 10^{18}$	6.0	1.33 ± 0.10	218 ± 3	Vernazza et al. (2021)
(94) Aurora	$3.22 \pm 0.91 \times 10^{18}$	28.1	0.82 ± 0.27	195.3 ± 10.1	Kretlow (2020)
(110) Lydia	$1.37 \pm 0.02 \times 10^{18}$	1.4	5.42 ± 1.62	78.5 ± 7.8	Kretlow (2020)
(223) Rosa	$9.48 \pm 6.98 \times 10^{16}$	73.6	0.26 ± 0.19	88.9 ± 2.6	Kretlow (2020)
(308) Polyxo	$3.05 \pm 0.26 \times 10^{18}$	8.5	2.74 ± 0.25	128.6 ± 1.6	Masiero et al. (2014)
(389) Industria	$6.80 \pm 0.24 \times 10^{17}$	3.6	2.58 ± 0.39	79.6 ± 3.9	Kretlow (2020)
(445) Edna	$5.24 \pm 0.11 \times 10^{17}$	2.1	1.51 ± 0.19	87.2 ± 3.7	Kretlow (2020)
(471) Papagena	$3.49 \pm 1.30 \times 10^{18}$	37.4	2.70 ± 1.08	135.1 ± 6.3	Kretlow (2020)
(712) Boliviana	$1.66 \pm 0.61 \times 10^{18}$	36.8	1.23 ± 0.46	136.9 ± 3.4	Kretlow (2020)

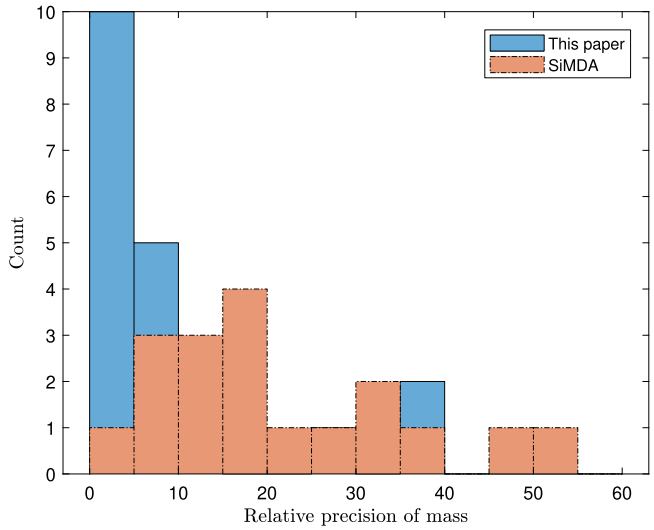

Figure 3. Histogram of the precision statistics for mass determination. The solid blue line represents the results of this paper and the dashed brown line represents the results of SiMDA.

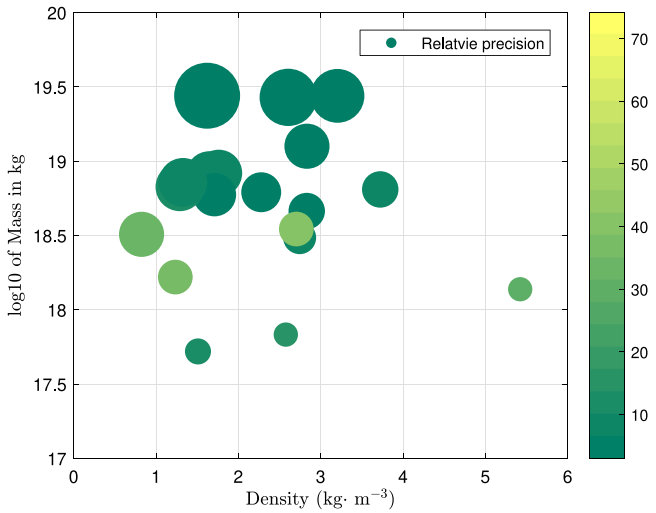

Figure 4. Mass vs. bulky density for 20 asteroids, with the color depth representing the precision of mass determination and the size of the circle representing the diameter.

density with the grain density, we can estimate the macroporosity of (445) Edna to be 33%.

4.3. Fisher Information as a Mass Uncertainty Indicator

The uncertainty of asteroid mass determination using close encounters is influenced by various factors, including the encounter conditions and the number and precision of the observations. In this study, we use Fisher information as an indicator to assess the effectiveness of mass determination. According to the Cramer–Rao lower bound (Nielsen 2013), we have

$$\boldsymbol{Var}(M) \geqslant \frac{1}{I(M)}. \tag{16}$$

A power-law function is employed to fit the relationship between the lower bound and the actual uncertainty in our analysis. Figure 5 shows the positive correlation between the lower bound and the actual uncertainty. This indicates that the Fisher information can serve as an indicator of uncertainty. And it is worth noting that the signal of the perturbation, as described in the algorithm to find close encounters by Siltala & Granvik (2020), is similar to Fisher information.

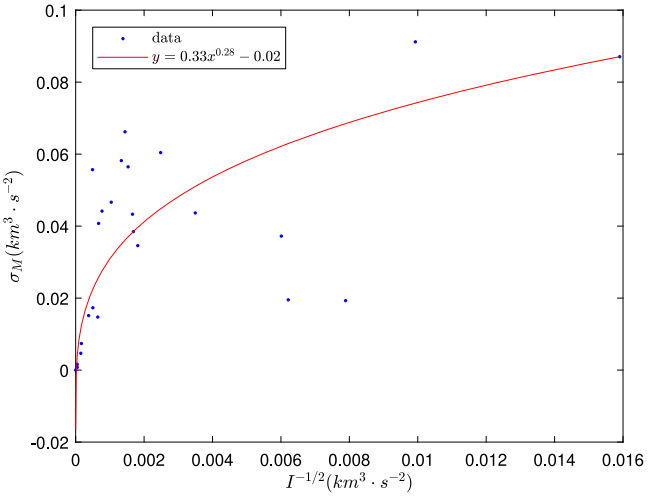

Figure 5. Relationship between the lower bound and the actual uncertainty.

In order to evaluate the impact of adding Gaia observations on the uncertainty of mass determination, we conducted calculations of Fisher information considering only ground-based observations. We then estimated the uncertainty using the power-law relationship mentioned earlier. It is important to note that this effect is highly complex and influenced by various factors, including the encounter conditions, precision and distribution of ground-based observations, precision and distribution of Gaia observations, and more.

It is found that encounters occurring within 2 yr from the Gaia intermediate observation epoch show minimal improvement in uncertainty. On the other hand, encounters occurring 3–5 yr from the Gaia intermediate observation epoch exhibit more significant improvements. This suggests that the perturbation resulting from the encounter requires time to be amplified and represented in the observations.

5. Conclusions

The masses of 20 asteroids are determined using ground-based observations in combination with Gaia DR3 observations. Though the total number is small as compared with the ground-based observations, the Gaia DR3 observations contribute significantly to the high precision determination. Meanwhile, in the mass determination method, considering the high precision of the Gaia observations, we use Fisher information to select appropriate model parameters on the one hand, and modify Encke's equation of motion to construct a complete dynamical model on the other hand. The results show that the use of Gaia DR3 data provides significant benefits in terms of asteroid mass determination. These provide methodological references for future mass determination using Gaia asteroid observations.

Acknowledgments

We are grateful for the very fruitful criticism by the anonymous referee. This work is financially supported by National Natural Science Foundation of China (grant Nos. 12103091, 11273066, 12203105). This research has made use of data provided by the International Astronomical Union's Minor Planet Center. We acknowledge the science research grants from the China Manned Space Project with NO.CMS-CSST-2021-A12, CMS-CSST2021-B10. This work has made use of data from the European Space Agency (ESA) mission Gaia (https://www.cosmos.esa.int/gaia), processed by the Gaia Data Processing and Analysis Consortium (DPAC, https://www.cosmos.esa.int/web/gaia/dpac/consortium). Funding for the DPAC has been provided by national institutions, in particular the institutions participating in the Gaia Multilateral Agreement.

Software: The code used in this article will be shared on reasonable request to the corresponding author.

ORCID iDs

Fan Li (李凡) https://orcid.org/0000-0002-2997-3098
Ye Yuan (袁烨) https://orcid.org/0000-0002-4686-8548
Jian Chen (陈健) https://orcid.org/0009-0006-9369-0806

References

Avdellidou, C., Pajola, M., Lucchetti, A., et al. 2021, A&A, 656, L18
Baer, J., & Chesley, S. R. 2017, AJ, 154, 76
Brown, P. G., Hildebrand, A. R., Zolensky, M. E., et al. 2000, Sci, 290, 320
Carpino, M., & Knezevic, Z. 1996, in IAU Symp. 172, Dynamics, Ephemerides, and Astrometry of the Solar System, ed. S. Ferraz-Mello, B. Morando, & B. Morando (New York: Springer), 203
Carry, B. 2012, P&SS, 73, 98
Farnocchia, D., Bellerose, J., Bhaskaran, S., Micheli, M., & Weryk, R. 2021a, Icar, 358, 114276
Farnocchia, D., Chesley, S. R., Chamberlin, A. B., & Tholen, D. J. 2015, Icar, 245, 94
Farnocchia, D., Chesley, S. R., Takahashi, Y., et al. 2021b, Icar, 369, 114594
Fienga, A., Laskar, J., Morley, T., et al. 2009, A&A, 507, 1675
Gaia Collaboration, Prusti, T., de Bruijne, J. H. J., et al. 2016, A&A, 595, A1
Gaia Collaboration, Spoto, F., Tanga, P., et al. 2018a, A&A, 616, A13
Gaia Collaboration, Brown, A. G. A., Vallenari, A., et al. 2018b, A&A, 616, A1
Gaia Collaboration, Vallenari, A., Brown, A. G. A., et al. 2023, A&A, 674, A1
Goffin, E. 2014, A&A, 565, A56
Hernandez, D. M., & Holman, M. J. 2021, MNRAS, 502, 556
Hiroi, T., Zolensky, M. E., & Pieters, C. M. 2001, Sci, 293, 2234
Hiroi, T., Kanno, A., Nakamura, R., et al. 2003, in 34th Annual Lunar and Planetary Science Conf. (League City, TX: LPI), 1425
Kretlow, M. 2020, in 14th Europlanet Science Congress (Strasbourg: EPSC)
Kretlow, M. 2022, A&A, 668, A141
Lehmann, E. L., & Casella, G. 1998, Theory of Point Estimation (New York: Springer)
Li, F., Fu, Y., & Yuan, Y. 2019, AJ, 157, 210
Ly, A., Marsman, M., Verhagen, J., Grasman, R., & Wagenmakers, E.-J. 2017, arXiv:1705.01064
Masiero, J. R., Grav, T., Mainzer, A. K., et al. 2014, ApJ, 791, 121
Michel, P., Benz, W., & Richardson, D. C. 2004, Icar, 168, 420
Nielsen, F. 2013, arXiv:1301.3578
OfekE. O. (2014) MATLAB Package for Astronomy and Astrophysics, Astrophysics Source Code Libraryascl:1407.005
Park, R. S., Folkner, W. M., Williams, J. G., & Boggs, D. H. 2021, AJ, 161, 105
Siltala, L., & Granvik, M. 2017, Icar, 297, 149
Siltala, L., & Granvik, M. 2020, A&A, 633, A46
Siltala, L., & Granvik, M. 2022a, A&A, 658, A65
Siltala, L., & Granvik, M. 2022b, in 16th Europlanet Science Congress (Strasbourg: EPSC)
Standish, M. 2000, in IAU Coll. 180: Towards Models and Constants for Sub-Microarcsecond Astrometry, ed. K. J Johnston et al. (Washington, DC: U.S. Naval Observator), 120
Tang, H. J., Li, F., & Fu, Y. N. 2017, AcASn, 58, 59
Tanga, P., Pauwels, T., Mignard, F., et al. 2023, A&A, 674, A12
Tegmark, M. 1997, PhRvL, 79, 3806
Urban, S. E., & Seidelmann, P. K. 2014, AAS Meeting Abstracts, 223, 247
Vereš, P., Farnocchia, D., Chesley, S. R., & Chamberlin, A. B. 2017, Icar, 296, 139
Vernazza, P., Ferrais, M., Jorda, L., et al. 2021, A&A, 654, A56
Yuan, Y., Li, F., Fu, Y., & Chen, J. 2021, A&A, 654, A66